4

# Texture Analysis Methods for Medical Image Characterisation

William Henry Nailon
*Department of Oncology Physics, Edinburgh Cancer Centre & School of Engineering, University of Edinburgh, United Kingdom*

## 1. Introduction

Texture analysis refers to the branch of imaging science that is concerned with the description of characteristic image properties by textural features. However, there is no universally agreed-upon definition of what image texture is and in general different researchers use different definitions depending upon the particular area of application (Tuceryan & Jain, 1998). In this chapter texture is defined as the spatial variation of pixel intensities, which is a definition that is widely used and accepted in the field. The main image processing disciplines in which texture analysis techniques are used are classification, segmentation and synthesis. In image classification the goal is to classify different images or image regions into distinct groups (Pietikainen, 2000). Texture analysis methods are well suited to this because they provide unique information on the texture, or spatial variation of pixels, of the region where they are applied. In image segmentation problems the aim is to establish boundaries between different image regions (Mirmehdi et al., 2008). By applying texture analysis methods to an image, and determining the precise location where texture feature values change significantly, boundaries between regions can be established. Synthesising image texture is important in three-dimensional (3D) computer graphics applications where the goal is to generate highly complex and realistic looking surfaces. Fractals have proven to be a mathematically elegant means of generating textured surfaces through the iteration of concise equations (Pentland, 1984). Conversely the ability to accurately represent a textured surface by a concise set of fractal equations has led to significant advances in image compression applications using fractal methods (Distani et al., 2006)

An example of image classification is presented in Fig. 1 in which it is possible to uniquely identify the two different textures (left, grass; right, water) by eye. In Fig. 2 the image on the left is a composite image formed from eight Brodatz textures, all of which are represented in approximately equal proportions. The right image is a grey-level texture map showing the ideal segmentation of the textures (Weber, 2004).

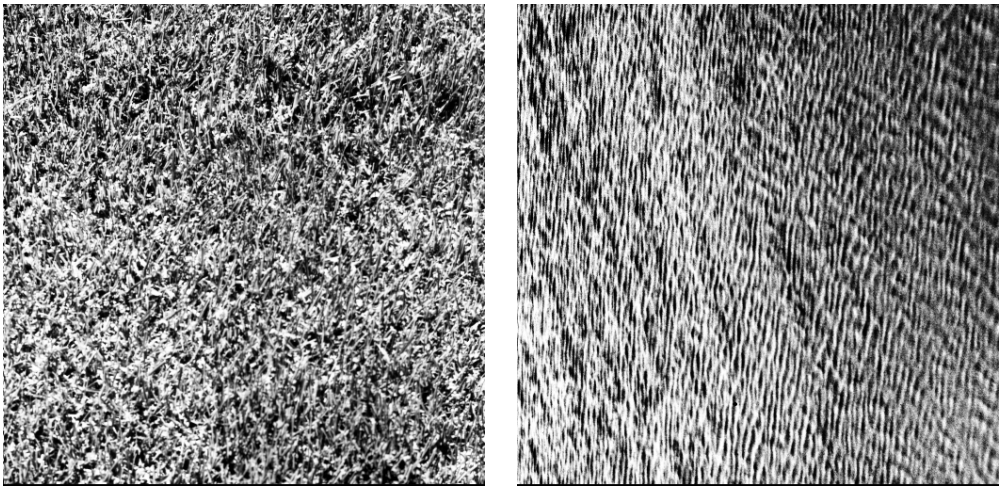

Fig. 1. Digital images of two visibly different textured regions extracted from the Brodatz texture database (Brodatz, 1966). Left, image of grass (1.2.01, D9 H.E.). Right, image of water (1.2.08, D38 H.E.) (Weber, 2004).

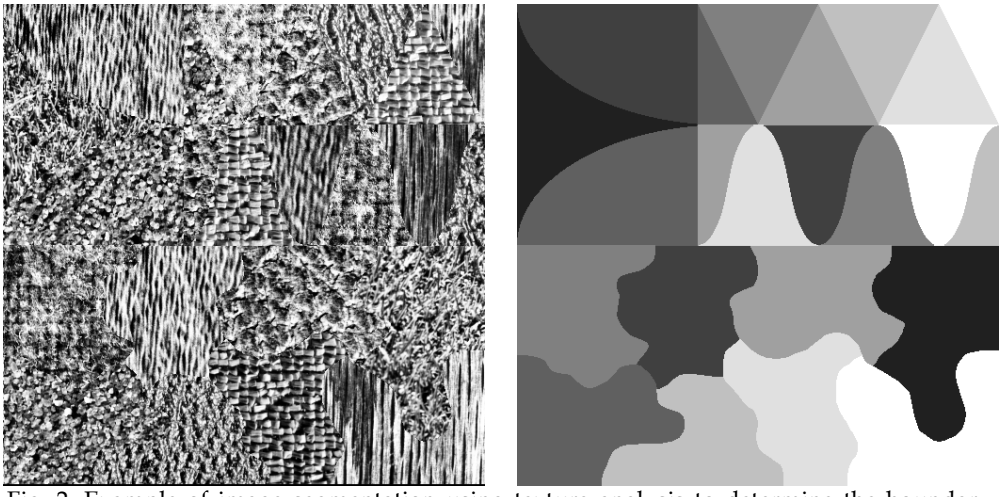

Fig. 2. Example of image segmentation using texture analysis to determine the boundary between distinct regions of texture. Left, mosaic image of eight Brodatz textures represented in approximately equal proportions. Right, grey-level texture map showing the ideal segmentation of the textures (Weber, 2004).

## 2. The Visual Perception of Texture

Much of our understanding of machine vision algorithms is a result of attempts to overcome the failings of the human visual system to detect certain textured patterns. This understanding has proven vital in evaluating and comparing the performance of human

vision against machine-based texture analysis approaches. Julesz, an experimental psychologist, was an early pioneer in the visual perception of texture (Julesz, 1975). He was responsible for establishing authoritative data on the performance of the human vision system at discriminating certain classes of texture. He verified that discriminating between two image textures depends largely upon the difference in the second-order statistics of the textures. That is, for two textures with identical second-order statistics a deliberate amount of effort is required to discriminate between them. In contrast little effort is required when the second-order statistics of the textures are different. However, this observation does not extend to textures that differ in third- or higher-order statistics, which are not readily discriminated by eye (Julesz, 1975). This is illustrated in Fig. 3 in which each of the main textured images (left and right) has a smaller area of similar, but subtly different, texture embedded within it. In the image on the left both the main and embedded areas have identical first-order statistics, however, their second-order statistics are different making it straightforward to discriminate both regions. In the image on the right both textures have identical first- and second-order statistics and therefore it is only after careful scrutiny that the different textured regions become visible.

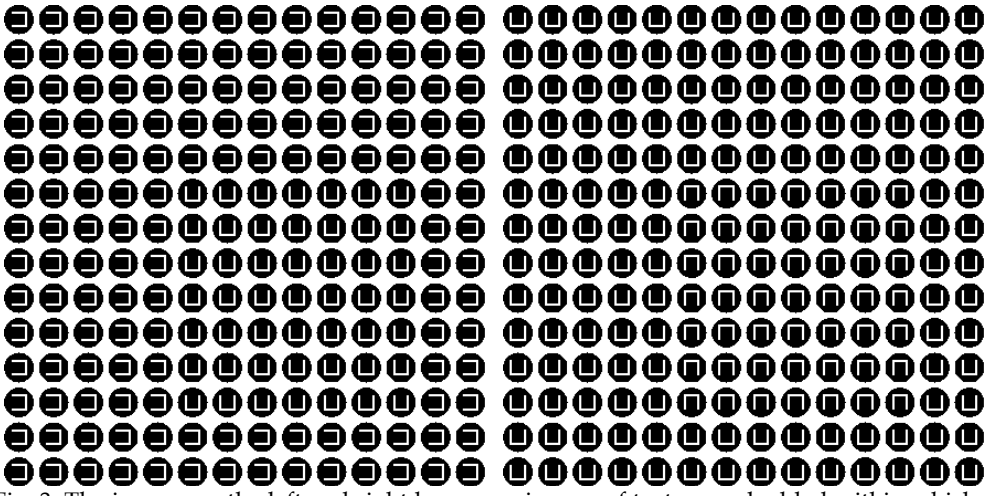

Fig. 3. The images on the left and right have a main area of texture embedded within which is a smaller area of similar, but subtly different, texture. In the left image both textures have the same first-order statistics and different second-order statistics, which makes it straightforward for an observer to distinguish between them. In the image on the right both textures have identical first- and second-order statistics and hence only after careful scrutiny are the different patterns visible (Julesz, 1975).

Although our understanding of the cognitive process of human vision is constantly expanding much has been learned from experiments in the visual perception of digital image information (Bruce et al, 2003). Such work is vital, particularly in medical imaging where the misinterpretation of image information can have a serious impact on health (ICRU, 1999). This is particularly apparent in radiotherapy, the treatment of cancer by ionising radiation, where the aim is to deliver as high a radiation dose as possible to

diseased tissue whilst limiting the radiation dose to healthy tissue. Delineation of the tumour volume is based primarily on visual assessment of computerised tomographic (CT) and magnetic resonance (MR) image data by a radiation oncologist. Accurately defining the tumour, and potential areas of tumour involvement, on CT and MR data is a complex image interpretation process requiring considerable clinical experience. As a result significant inter- and intra-clinician variability has been reported in the contouring of tumours of the lung, prostate, brain and oesophagus (Weltens et al., 2001; Steenbakkers et al., 2005). This variability has been shown to be significant and heavily correlated with the digital imaging modality used and the image settings applied during the assessment.

Texture analysis is presented here as a useful computational method for discriminating between pathologically different regions on medical images because it has been proven to perform better than human eyesight at discriminating certain classes of texture (Julesz, 1975). Section 3 presents statistical texture analysis through first-, second-, and higher-order techniques. Section 4 considers the use of fractal methods for characterising image texture through the box-counting and Korcak techniques. In section 5 methods are presented for improving the overall efficiency of the texture analysis approach. These are feature selection, reduction and classification. Section 6 presents two case studies, which demonstrate the use of these approaches in practical biomedical imaging.

## 3. Statistical Approaches for Texture Analysis

To examine an image using texture analysis the image is treated as a 3D textured surface. This is illustrated in Fig. 4 which shows the textured intensity surface representation of a two-dimensional (2D) medical image. In first-order statistical texture analysis, information on texture is extracted from the histogram of image intensity. This approach measures the frequency of a particular grey-level at a random image position and does not take into account correlations, or co-occurrences, between pixels. In second-order statistical texture analysis, information on texture is based on the probability of finding a pair of grey-levels at random distances and orientations over an entire image. Extension to higher-order statistics involves increasing the number of variables studied.

Many conventional approaches used to study texture have concentrated on using 2D techniques to compute features relating to image texture. This traditional approach has been used extensively to describe different image textures by unique features and has found application in many disparate fields such as: discrimination of terrain from aerial photographs (Conners & Harlow, 1980); in vitro classification of tissue from intravascular ultrasound (Nailon, 1997); identification of prion protein distribution in cases of Creutzfeld-Jakob disease (CJD) (Nailon & Ironside, 2000); classification of pulmonary emphysema from lung on high-resolution CT images (Uppaluri et al., 1997; Xu et al., 2004; Xu et al., 2006); and identifying normal and cancerous pathology (Karahaliou et al., 2008, Zhou et al., 2007; Yu et a., 2009). Higher-order approaches have been used to localise thrombotic tissue in the aorta (Podda, 2005) and to determine if functional vascular information found in dynamic MR sequences exists on anatomical MR sequences (Winzenrieth, 2006). Extension of these approaches to 3D is continuing to develop within the machine vision community. Several authors have reported the application of 2D texture analysis methods on a slice-by-slice

basis through volumetric data, however, it has been reported that with this approach information may be lost (Kovalev et al., 2001; Kurani et al., 2004). Findings reported by Xu et al., on the use of 3D textural features for discriminating between smoking related lung pathology, demonstrate the power of this approach for this particular application (Xu et al., 2006). Kovalev et al., showed that an extended 3D co-occurrence matrix approach can be used for the classification and segmentation of diffuse brain lesions on MR image data (Kovalev et al., 2001). Texture analysis has also been used to identify unique pathology on multi-modality images of cancer patients. Using the local binary operator to analyse the weak underlying textures found in transrectal ultrasound images of the prostate, Kachouie and Fieguth demonstrated that the approach was suitable for segmentation of the prostate (Kachouie & Fieguth, 2007). In another cancer-related study of 48 normal images and 58 cancer images of the colon, Esgiar et al., demonstrated that by adding a fractal feature to traditional statistical features the sensitivity of the classification improved (Esgiar et al., 2002).

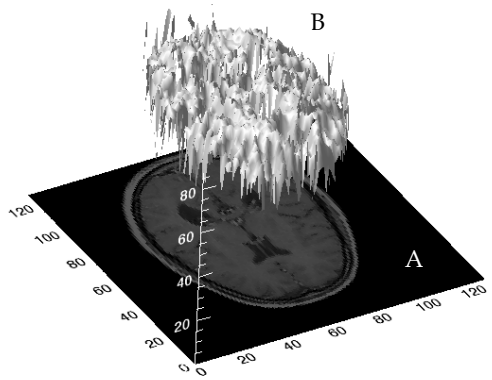


Fig. 4. Three-dimensional textured intensity surface representation of a medical image. **A**: Two-dimensional MR image of the brain. **B**: Pixel values of the MR image plotted on the vertical axis to produce a 3D textured surface.

With the proliferation of 3D medical image data of near isotropic quality there is an increasing demand for artificial intelligence methods capable of deriving quantitative measures relating to distinct pathology. The remaining sections of this chapter provide a review of statistical and fractal texture analysis approaches in the context of medical imaging and provide comprehensive real-world examples, in the form of two case studies, on the use of these approaches in clinical practice. In case study 1 texture analysis is presented as a means of classifying distinct regions in cancer images, which could be developed further towards automatic classification. In case study 2 texture analysis is presented as an objective means of identifying the different patterns of prion protein found in variant CJD (vCJD) and sporadic CJD. Two contrasting methods are presented in the case studies for evaluating the performance of the texture analysis methodologies.

### 3.1 First-Order Statistical Texture Analysis

First-order texture analysis measures use the image histogram, or pixel occurrence probability, to calculate texture. The main advantage of this approach is its simplicity through the use of standard descriptors (e.g. mean and variance) to characterise the data (Press, 1998). However, the power of the approach for discriminating between unique textures is limited in certain applications because the method does not consider the spatial relationship, and correlation, between pixels. For any surface, or image, grey-levels are in the range $0 \le i \le N_g - 1$, where $N_g$ is the total number of distinct grey-levels. If $N(i)$ is the number of pixels with intensity $i$ and $M$ is the total number of pixels in an image, it follows that the histogram, or pixel occurrence probability, is given by,

$$P(i) = \frac{N(i)}{M}. \tag{1}$$

In general seven features commonly used to describe the properties of the image histogram, and therefore image texture, are computed. These are: mean; variance; coarseness; skewness; kurtosis; energy; and entropy.

### 3.2 Second-Order Statistical Texture Analysis

The human visual system cannot discriminate between texture pairs with matching second-order statistics (see Fig. 3) (Julesz, 1975). The first machine-vision framework for calculating second-order or pixel co-occurrence texture information was developed for analysing aerial photography images (Haralick et al., 1973). In this technique pixel co-occurrence matrices, which are commonly referred to as grey-tone spatial dependence matrices (GTSDM), are computed. The entries in a GTSDM are the probability of finding a pixel with grey-level $i$ at a distance $d$ and angle $\alpha$ from a pixel with a grey-level $j$. This may be written more formally as $P(i, j : d, \alpha)$. An essential component of this framework is that each pixel has eight nearest-neighbours connected to it, except at the periphery. As a result four GTSDMs are required to describe the texture content in the horizontal $(P_H = 0^0)$, vertical $(P_V = 90^0)$ right- $(P_{RD} = 45^0)$ and left-diagonal $(P_{LD} = 135^0)$ directions. This is illustrated in Fig. 5.

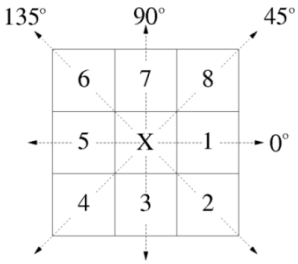


Fig. 5. Eight nearest-neighbour pixels used in the GTSDM framework to describe pixel connectivity. Cells 1 and 5 show the horizontal $(P_H)$, 4 and 8 the right-diagonal $(P_{RD})$, 3 and 7 the vertical $(P_V)$ and 2 and 6 the left-diagonal $(P_{LD})$ nearest-neighbours.

An example of the calculation of a horizontal co-occurrence matrix $(P_H)$ on a $4\times4$ image containing four unique grey-levels is shown in Fig. 6. A complete representation of image texture is contained in the co-occurrence matrices calculated in the four directions. Extracting information from these matrices using textural features, which are sensitive to specific elements of texture, provides unique information on the structure of the texture being investigated. Haralick et al., proposed a set of 14 local features specifically designed for this purpose (Haralick et al., 1973). In practice the information provided by certain features may be highly correlated or of limited practical use. A feature selection strategy is therefore useful with this approach to take account of redundant, or irrelevant, information. This is discussed in more detail in section 5. It is also interesting to note that prior to any processing the GTSDMs, which are symmetric, can provide some useful information on the characteristics of the image being studied. For example, the co-occurrence matrix entries for a coarse texture will be heavily focused along the diagonals relative to the distance $d$ between the pixels studied.

| | | | |
|---|---|---|---|
| 0 | 2 | 2 | 2 |
| 0 | 3 | 2 | 2 |
| 1 | 2 | 2 | 2 |
| 3 | 0 | 3 | 0 |

$(P_H)$

| Grey-Level | 0 | 1 | 2 | 3 |
|---|---|---|---|---|
| 0 | 0 | 0 | 1 | 4 |
| 1 | 0 | 0 | 1 | 0 |
| 2 | 1 | 1 | 10 | 1 |
| 3 | 4 | 0 | 1 | 0 |

Fig. 6. Simple example demonstrating the formation of a co-occurrence matrix from an image. Left, $4\times4$ image with four unique grey-levels. Right, the resulting horizontal co-occurrence matrix $(P_H)$.

To illustrate the computational requirements of this framework, three of the 14 features proposed by Haralick et al., (Haralick et al., 1973) are presented in equations 2 to 4.

Angular second moment,

$$f_1 = \sum_{i=1}^{N_q}\sum_{j=1}^{N_q} p'(i,j)^2. \tag{2}$$

Contrast,

$$f_2 = \sum_{i=0}^{N_q-1} n^2 \left[ \sum_{i=1}^{N_q}\sum_{j=1}^{N_q} p'(i,j) \right]_{i-j=n}. \tag{3}$$

Correlation,

$$f_3 = \sum_{i=1}^{N_q}\sum_{j=1}^{N_q} \frac{(i-\mu_x)(j-\mu_y)p'(i,j)}{\sigma_x\sigma_y}, \tag{4}$$

where, $N_q$ is the number of distinct grey-levels in the input and $\mu_x, \mu_y, \sigma_x$ and $\sigma_y$ are the means and standard deviations of $p'(i,j)$. Throughout, $p'(i,j) = P(i,j)/R$, where $P(i,j)$ is the average of $(P_H + P_V + P_{LD} + P_{RD})$ and R is the maximum number of resolution cells in a GTSDM.

### 3.3 Higher-Order Statistical Texture Analysis

The grey-level run length method (GLRLM) is based on the analysis of higher-order statistical information (Galloway, 1975). In this approach GLRLMs contain information on the run of a particular grey-level, or grey-level range, in a particular direction. The number of pixels contained within the run is the run-length. A coarse texture will therefore be dominated by relatively long runs whereas a fine texture will be populated by much shorter runs. The number of runs $r'$ with gray-level $i$, or lying within a grey-level range $i$, of run-length $j$ in a direction $\alpha$ is denoted by $R(\alpha) = [r'(i,j \mid \alpha)]$. This is analogous to the GTSDM technique (Haralick et al., 1973) as four GTRLMs are commonly used to describe texture runs in the directions $(0^0, 45^0, 90^0 \text{ and } 135^0)$ on linearly adjacent pixels. An example of the calculation of a horizontal GLRLM is shown in Fig. 7.

| | | | |
|---|---|---|---|
| 0 | 1 | 2 | 2 |
| 0 | 3 | 2 | 2 |
| 1 | 2 | 2 | 2 |
| 3 | 0 | 3 | 0 |

| Grey-Level \ Run-Length | $0^0$ | 1 | 2 | 3 | 4 |
|---|---|---|---|---|---|
| | 0 | 4 | 0 | 0 | 0 |
| | 1 | 2 | 0 | 0 | 0 |
| | 2 | 0 | 2 | 1 | 0 |
| | 3 | 3 | 0 | 0 | 0 |

Fig. 7. Simple example demonstrating the formation of a GLRLM. Left, $4 \times 4$ image with four unique grey-levels. Right, the resulting GLRLM in the direction $0^0$.

A set of seven numerical texture measures are computed from the GTRLMs. Three of these measures are presented here to illustrate the computation of feature information using this framework.

Short Run Emphasis,

$$f_{SR} = \frac{1}{T_R} \sum_{i=0}^{N_g - 1} \sum_{j=1}^{N_r} \frac{r'(i,j \mid \alpha)}{j^2}. \tag{5}$$

Long Run Emphasis,

$$f_{LR} = \frac{1}{T_R} \sum_{i=0}^{N_g - 1} \sum_{j=1}^{N_r} j^2 r'(i,j \mid \alpha). \tag{6}$$

Grey-Level Distribution,

$$f_{GD} = \frac{1}{T_R} \sum_{i=0}^{N_g-1} \left[ \sum_{j=1}^{N_r} r'(i,j \mid \alpha) \right]^2, \tag{7}$$

where $N_g$ is the maximum number of grey-levels, $N_r$ is the number of different run lengths in the matrix and,

$$T_R = \sum_{i=0}^{N_g-1} \sum_{j=1}^{N_r} r'(i,j \mid \alpha). \tag{8}$$

$T_R$ serves as a normalising factor in each of the run length equations.

### 3.4 Fourier Power Spectrum

Two-dimensional transforms have been used extensively in image processing to tackle problems such as image description and enhancement (Pratt, 1978). Of these, the Fourier transform is one of the most widely used (Gonzalez and Woods, 2001). Fourier analysis can be used to study the properties of textured scenes, for example the power spectrum reveals information on the coarseness/fineness (periodicity) and directionality of a texture. Texture directionality is preserved in the power spectrum because it allows directional and non-directional components of the texture to be distinguished (Bajscy, 1973). These observations have given rise to two powerful approaches for extracting texture primitives from the Fourier power spectrum, namely, ring and wedge filters. Working from the origin of the power spectrum the coarseness/fineness is measured between rings of inner radius $r_1$ and $r_2$ . The size of the rings can be varied according to the application. The directionality of the texture is found by measuring the average power over wedge-shaped regions centred at the origin of the power spectrum. The size of the wedge $\phi_w = \phi_1 - \phi_2$ depends upon the application. Fig. 8 illustrates the extraction of ring and wedge filters from the Fourier power spectrum of a $32 \times 32$ test image consisting of black pixels everywhere except for a $3 \times 3$ region of white pixels centred at the origin.

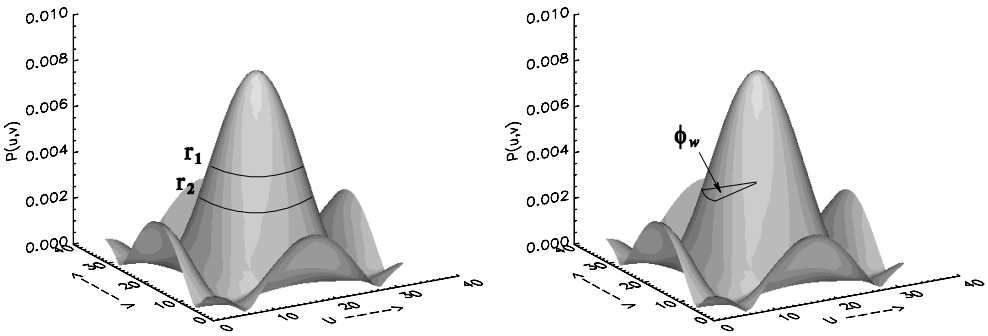


Fig. 8. Fourier power spectrum showing the extraction of ring and wedge filters. The spectrum was generated on a $32 \times 32$ test image consisting of black pixels everywhere except for a $3 \times 3$ region of white pixels centred at the origin.

In image analysis the Fourier transform $F(u,v)$ is considered in its discrete form and the power spectrum $P(u,v)$ is calculated from,

$$P(u,v) = \left|F(u,v\right|^2. \tag{9}$$

The average power contained in a ring centred at the origin with inner and outer radii $r_1$ and $r_2$ respectively, is given by the summation of the contributions along the direction $\phi$ ,

$$P(r) = 2\sum_{\phi=0}^{\pi} P(r,\phi). \tag{10}$$

The contribution from a wedge of size $\phi_w$ is found from summation of the radial components within the wedge boundaries. That is,

$$P(\phi_w) = \sum_{r=0}^{n/2} P(r,\phi), \tag{11}$$

where $n$ is the window size.

## 4. Fractal Texture Analysis

Until the introduction of fractals it was difficult to accurately describe, mathematically, complex real-world shapes such as mountains, coastlines, trees and clouds (Mandelbrot, 1977). Fractals provide a succinct and accurate method for describing natural objects that would previously have been described by spheres, cylinders and cubes. However, these descriptors are smooth, which makes modelling irregular natural scenes, or surfaces, very difficult. The popularity of fractals has grown considerably over the past three decades since the term was first coined by Mandelbrot to describe structures too complex for Euclidean geometry to describe by a single measure (Mandelbrot, 1977). The fractal dimension describes the degree of irregularity or texture of a surface. With this approach rougher, or more irregular, structures have a greater fractal dimension (Feder, 1988; Peitgen & Saupe, 1988; Peitgen et al., 1992).

The property of self-similarity is one of the central concepts of fractal geometry (Turcotte, 1997). An object is self-similar if it can be decomposed into smaller copies of itself. This fundamental property leads to the classification of fractals into two distinct groups, random and deterministic. A good example of self-similarity is exhibited by an aerial image of an irregular coastline structure that has the same appearance within a range of magnification factors. At each magnification the coastline will not look exactly the same but only similar. This particular feature is common to many classes of real-life random fractals, which are not exactly self-similar. These are referred to as being statistically self-similar. In contrast, objects that do not change their appearance when viewed under arbitrary magnification are termed strictly self-similar. These are termed deterministic fractals due to their consistency over a range of magnification scales. The fractal dimension describes the disorder of an

object numerically, which in a sense is similar to the description of objects using standard Euclidean geometry. That is, the higher the dimension the more complicated the object. However, fractal descriptors allow the description of objects by non-integer dimensions.

A variety of techniques are used to estimate the fractal dimension of objects which, despite providing the same measure, can produce different fractal dimension values for analysis of the same object. This is due to the unique mechanism used by each technique to find the fractal dimension (Peitgen et al., 1992; Turcotte, 1997). Two approaches commonly used to calculate the fractal dimension of an image are discussed. The first is the box-counting approach (Peitgen et al., 1992). The second, which treats the input as a textured surface by plotting the intensity at each $x$ and $y$ position in the $z$ plane, calculates the fractal dimension using the Korcak method (Russ, 1994).

### 4.1 Fractal Dimension from Box-Counting

The box-counting dimension is closely related to the concept of self-similarity where a structure is sub-divided into smaller elements, each a smaller replica of the original structure. This sub-division characterises the structure by a self-similarity, or fractal, dimension and is a useful tool for characterising apparently random structures. This approach has been adopted in a variety of applications, for example in the characterisation of high resolution satellite images (Yu et al., 2007) and in the detection of cracks in CT images of wood (Li & Qi, 2007). The box-counting dimension $D_b$ of any bounded subset of $A$ in $\mathbf{R}^n$, which is a set in Euclidean space, may be formally defined as follows (Stoyan & Stoyan, 1994; Peitgen & Saupe, 1988). Let $N_r(A)$ be the smallest number of sets of $r$ that cover $A$. Then,

$$D_b(A) = \lim_{r \to 0} \frac{\log N_r(A)}{\log(1/r)}, \tag{12}$$

provided that the limit exists. Subdividing $\mathbf{R}^n$ into a lattice of grid size $r \times r$ where $r$ is continually reduced, it follows that $N'_r(A)$ is the number of grid elements that intersect $A$ and $D_b(A)$ is,

$$D_b(A) = \lim_{r \to 0} \frac{\log N'_r(A)}{\log(1/r)}, \tag{13}$$

provided that the limit exists. This implies that the box counting dimension $D_b(A)$ and $N_r(A)$ are related by the following power law relation,

$$N_r(A) = \frac{1}{r^{D_b(A)}}. \tag{14}$$

Proof of this relation can be obtained by taking logs of both sides of equation (14) and rearranging to form equation (15),

$$\log N_r(A) = D_b(A)\log(1/r). \tag{15}$$

From equation (15) it is possible to make an analogy to the equation of a straight line, $y = mx + c$, where $m$ is the slope of the line and $c$ is the $y$ intersect. The box-counting dimension is implemented by placing a bounded set $A$, in the form of a medical image, on to a grid formed from boxes of size $r \times r$. Grid boxes containing some of the structure, which in the case of a medical image is represented by the grey-levels within a certain range, are next counted. The total number of boxes in the grid that contain some of the structure is $N_r(A)$. The algorithm continues by altering $r$ to progressively smaller sizes and counting $N_r(A)$. The slope of the line fitted through the plot of $\log(1/r)$ against $\log(N_r(A)$ is the fractal, or box-counting, dimension of the medical image region under investigation.

### 4.2 Korcak Fractal Analysis

This approach uses the idea of a cross-section, or zeroset, through the surface or image to determine the fractal dimension (Russ, 1994). It is implemented by passing a horizontal plane through a 3 D surface in a vertical direction to produce an intersection profile. The points of the surface that lie above the horizontal plane are commonly referred to as islands and the remaining areas of the plane are lakes. This is equivalent to applying a threshold and measuring the area of the islands and lakes that lie above or below the surface. This is illustrated in Fig. 9 which shows the result of repeated thresholding on an image of the cerebellum for a case of vCJD. A log-log plot of the number of islands, or lakes, whose area exceeds $A$ is fitted to a straight line (see Fig. 10). The slope of this line is used to calculate the fractal dimension. This approach is termed the Korcak method (Russ, 1994).

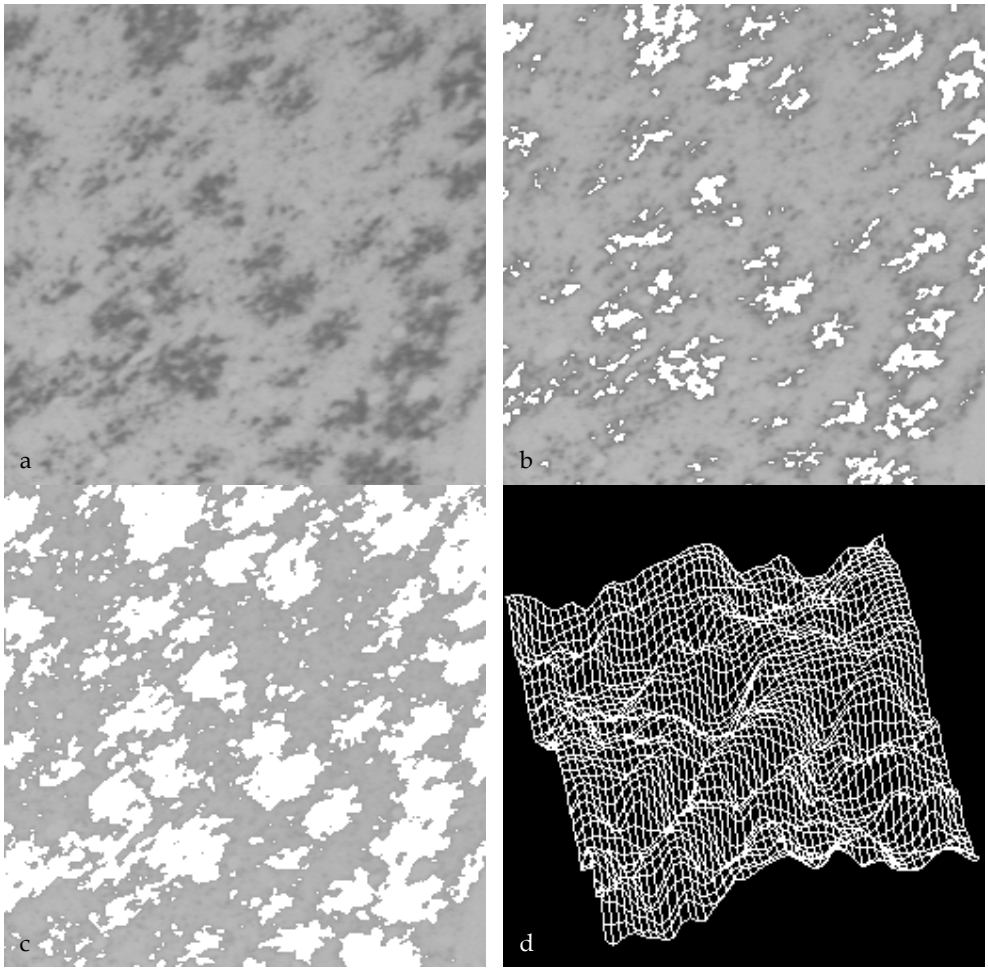


Fig. 9. **a**: Microscopic image showing the widespread deposition of prion protein in the cerebellum of a vCJD case. **b** and **c**: The result of repeated grey-level thresholding. **d**: The image surface cut by a plane or zeroset. Repeating the thresholding at many levels and constructing a Korcak plot of the cumulative number of islands provides a measure of the fractal dimension.

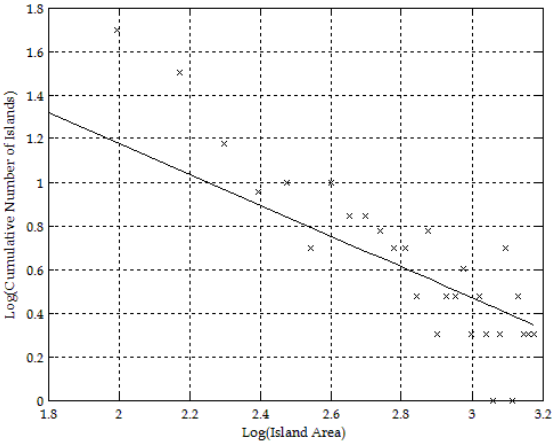


Fig. 10. Plot of fractal island area against cumulative number of islands acquired within the area. The slope of the straight line plotted through the data is used to determine the fractal dimension.

## 5. Feature Selection, Reduction and Classification

The texture analysis approaches presented in the preceding sections calculate features that describe properties of the image, or region, being studied. This information is next used in a pattern recognition system to classify the objects, or texture patterns of interest, into an appropriate number of categories or classes (Therrien, 1989). However, some of the features calculated may be highly correlated and some may contain irrelevant information. Feature selection is used to select a subset of features $\boldsymbol{s}_p$ from a given set of $\boldsymbol{p}$ features such that $\boldsymbol{s}_p \leq \boldsymbol{p}$ and there is no significant degradation in the performance of the classification system (Therrien, 1989; Zongker & Jain, 1996; Stearns, 1976). The reduction of the feature set reduces the dimensionality of the classification problem and in some cases can increase the performance of the classification accuracy due to finite sample size effects (Jain & Chandrasekaran, 1982). Two powerful methods for reducing the number of features are presented. These are the sequential forward search (SFS) algorithm and its backward counterpart the sequential backward search (SBS) algorithm (Devijver & Kittler, 1982). The pattern recognition system must also be capable of partitioning, or clustering, the reduced feature set into classes of similar observations. The *K*-means algorithm belongs to the collection of multivariate methods used for classifying, or clustering, data and is presented because of its general applicability in classification problems (Therrien, 1989).

### 5.1 Feature Selection Using the Sequential Forward Search Algorithm

The SFS algorithm is a bottom-up strategy for removing redundant or irrelevant features from the feature matrix (Devijver & Kittler, 1982). At each successive iteration the feature that produces the largest value of the selection criterion function $J$ is added to the current feature set. Given a set of candidate features $Y \in \boldsymbol{R}$, a subset $X \in \boldsymbol{R}$ is selected without

significant degradation to the classification system (Jain & Zongker, 1997). The best subset $X$,

$$X = \{x_i \mid i = 1,2,\ldots,d, \quad x_i = Y\}, \tag{16}$$

of $d$ features where $(d \le D)$ is selected from the set,

$$Y = \{y_1 \mid j = 1,2,\ldots,D\}, \tag{17}$$

by optimising the criterion function $J$, chosen here to be the estimated minimum probability of error. For the set of measurements taken from $Y$, ideally the probability of correct classification $(\xi)$, with respect to any other combination, is given by,

$$\Xi = \{\xi_i \mid i = 1,2,\ldots,d\}. \tag{18}$$

It follows that the minimum probability of error for the space spanned by $\xi$, for each class $\omega_i$ is defined as,

$$E(\Xi) = \int [1 - \max(P(\omega_i \mid \xi))] p(\xi) d(\xi), \tag{19}$$

and the desired criterion function,

$$J(X) = \min(E(\Xi)). \tag{20}$$

One of the disadvantages of the SFS approach is that it may suffer from nesting. That is, because features selected and included in the feature subset cannot be removed, already selected features determine the course of the remaining selection process. This has noticeable hazards since after further iterations a feature may become superfluous. Another limitation of the SFS approach is that in the case of two feature variables, which alone provide little discrimination but together are very effective, the SFS approach may never detect this combination. To overcome this problem it is useful to start with a full set of available features and eliminate them one at a time. This is the method adopted by the SBS approach described in section 5.2.

### 5.2 Feature Selection Using the Sequential Backward Search Algorithm

The SBS is a top down approach, which starts with the complete feature set and removes one feature at each successive iteration (Devijver & Kittler, 1982). The feature that is chosen to be removed is the feature that results in the smallest reduction in the value of the selection criterion function when it is removed. In general, the SBS algorithm requires more computation than the SFS algorithm because initially it considers the number of features in the complete set as forming the subset. Although the SBS overcomes some of the difficulties of the SFS approach the resulting feature subset is not guaranteed to be optimal. Furthermore, like its counterpart the SBS algorithm suffers from nesting because once a feature is selected it cannot be disregarded. Implementation of the SBS approach is analogous to the SFS approach detailed in section 5.1. The SBS algorithm is computationally more expensive than the SFS algorithm, however, their performance is comparable. Despite

the shortcomings of the SFS and SBS techniques they are powerful techniques for reducing the feature set of real-world pattern recognition problems (Nouza, 1995).

### 5.3 Classification Using the *K*-means Algorithm

The general clustering problem is one of identifying clusters, or classes, of similar points. For the specific problem presented in this chapter this would involve clustering the features calculated on a specific image region into a unique cluster. The number of classes may be known or unknown depending on the particular problem. The *K*-means algorithm belongs to the collection of multivariate methods used for clustering data (Therrien, 1989; Hartigan, 1975; Duda et al., 2001). The algorithm starts with a partition of the observations into clusters. At each step the algorithm moves a case from one cluster to another if the move will increase the overall similarity within clusters. The algorithm ceases when the similarity within clusters can no longer be increased.

Assuming that the number of clusters $N_c$ is known in advance the *K*-means technique may be defined by the following three stages.

*Stage 1* – *Initialisation*: For the set of observations $\boldsymbol{Y} = \{\boldsymbol{y}_1, \boldsymbol{y}_2 \ldots, \boldsymbol{y}_N\}$ to be classified into the set of classes $\Omega = \{\omega_1, \omega_2, \ldots, \omega_{Nc}\}$, the algorithm starts with an arbitrary partition of the observations into $N_c$ clusters and computes the mean vector of each cluster $(\mu_1, \mu_2, \ldots \mu_{Nc})$ using the Euclidean distance $\|\boldsymbol{y}_i - \boldsymbol{\mu}_k\|^2$ where $\boldsymbol{\mu}_k$ is the sample mean of the $k^{th}$ cluster.

*Stage 2* - *Nearest Mean*: Assign each observation in $\boldsymbol{Y}$ to the cluster with the closest mean.

*Stage 3* - *Update and Repeat*: Update the mean vector for each cluster and repeat *Stage 2* until the result produces no significant change in the cluster means.

## 6. Biomedical Image Analysis Case Studies

Two case studies are presented to demonstrate the practical application of the texture analysis methods discussed in the previous sections. In the first, a texture analysis approach was used to classify regions of distinct pathology on CT images acquired on eight bladder cancer patients. In the second, texture analysis was used to study the distribution of abnormal prion protein found in the molecular layer of the cerebellum of cases of vCJD and sporadic CJD.

### 6.1 Case Study 1 - Texture Analysis of Radiotherapy Planning Target Volumes

The goal of radiotherapy, the treatment of cancer with ionising radiation, is to deliver as high a dose of radiation as possible to diseased tissue whilst sparing healthy tissue. In curative (radical) radiotherapy planning, delineation of the gross tumour volume (GTV) is primarily based on visual assessment of CT images by a radiation oncologist (Meyer, 2007). The accuracy therefore of the GTV is dependent upon the ability to visualise the tumour and as a result significant inter- and intra-clinician variability has been reported in the contouring of tumours of the prostate, lung, brain and oesophagus (Weltons et al., 2001; Steenbakkers et al., 2005).

The aim of the work presented in this case study was to develop a texture analysis methodology capable of distinguishing between the distinct pathology of the GTV and other clinically relevant regions on CT image data. For eight bladder patients (six male and two female), CT images were acquired at the radiotherapy planning stage and thereafter at regular intervals during treatment. All CT scans were acquired on a General Electric single slice CT scanner (IGE HiSpeed Fx/I, GE Medical Systems, Milwaukee, WI, USA). Seven patients were scanned with a 3 mm slice thickness and one patient with a 5 mm slice thickness. The repeat CT scans were registered against the corresponding planning reference CT scan to allow comparison of the same region on each image. Image features based on: the first-order histogram $(N = 7)$; second-order GTSDM $(N = 14)$; higher-order GLRLM $(N = 5)$; and a bespoke box-counting fractal approach $(N = 1)$ were calculated on pre-identified regions of the CT images of each patient (Nailon et al., 2008). Two classification environments were used to assess the performance of the approach in classifying the bladder, rectum and a region of multiple pathology on the axial, coronal and sagittal CT image planes. These were, in the first using all of the available features $(N = 27)$ and in the second using the best three features identified by the SFS approach. The classification results achieved are presented in Fig. 11. No significant discrimination was observed between the bladder, rectum and the region of multiple pathology on the axial, coronal and sagittal CT data using all of the available features $(N = 27)$. This is shown on the left column of Fig. 11. On the contrary, using the three best features identified by the SFS feature reduction approach, significant discrimination between the three pathological groups was possible. This is shown on the right column of Fig. 11. These results demonstrate the significant improvement in classification that can be achieved by removing features with little discriminatory power. Moreover the results demonstrate the effectiveness of texture analysis for classifying regions of interest, which may be difficult for the human observer to interpret.

The features that were found to work best were all from the GTSDM approach. The feature produced by the bespoke box-counting fractal approach was not found to have significant discriminatory power. However, more research is required into the use of fractal methods in this application area, particularly because assigning a single dimension to a whole region may not be appropriate (Mandelbrot, 1977). Furthermore, the fractal dimension calculation may have been influenced by the different distribution of grey-levels in the images due to variations in the amount of urine in the bladder and air in the rectum.

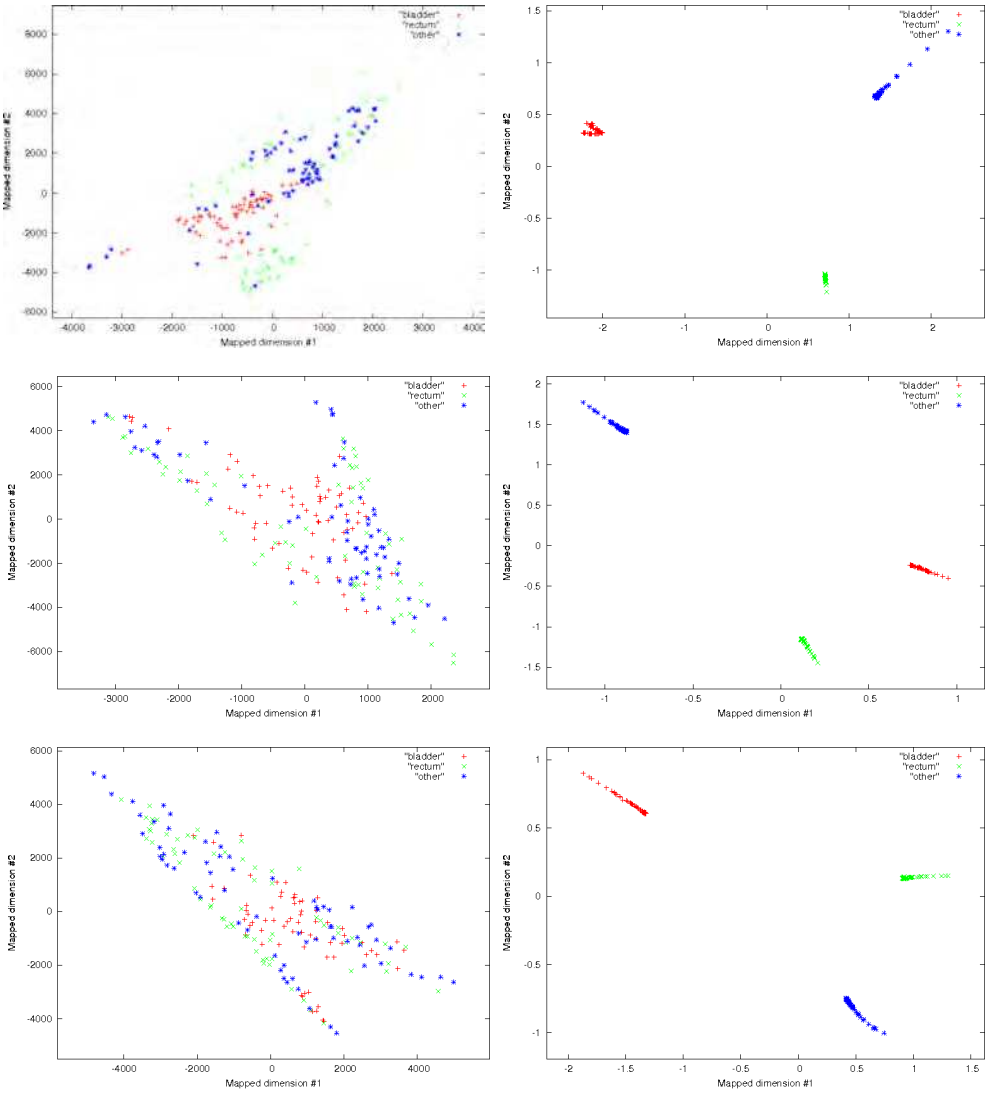


Fig. 11. Classification of the bladder, rectum and a region of multiple pathology identified as other on axial CT images through the pelvis using a texture analysis approach. Left (top: axial, middle: coronal, bottom: sagittal) plots showing the result of using all available features to classify the bladder, rectum and other. Right (top: axial, middle: coronal, bottom: sagittal) plots showing classification of the bladder, rectum and other using the best three features identified by the SFS approach. Sammon mapping was used to generate 2D representations of the multi-dimensional feature space and aid visualisation (Sammon, 1969).

The approach was also found to be insensitive to CT resolution and slice thickness for the data set studied. It was also noticed that discrimination of the bladder, rectum and other region in the coronal and sagittal image planes was comparable to the discrimination obtained in the axial plane. This is encouraging given that the coronal and sagittal data sets were produced from the axial data and suffer a loss of resolution because of finite CT slice thickness in the axial data acquisition procedure.

### 6.2 Case Study 2 – Prion Protein Characterisation Using Texture Analysis

Prion diseases are a group of fatal neurodegenerative diseases that occur in both animals and man (Bastian, 1991). Human prion diseases occur in sporadic, acquired and familial forms, the commonest of which is CJD (Ironside, 1998). The accumulation of prion protein within the brain is a cardinal feature of these diseases and can be identified by immunocytochemistry (Ironside et al., 2000). In this case study immunocytochemically stained sections were imaged using a Leica DMR microscope (Leica Microscopy Systems GmbH) and texture analysis techniques were applied to study the distribution of prion protein on the images acquired.

Formalin-fixed paraffin embedded tissue blocks were selected from the cerebellum of five cases of vCJD and seven cases of sporadic CJD with known codon 129 genotype and biochemical subtype (four cases of sporadic CJD methionine homozygotes type 1 and three cases of sporadic CJD methionine homozygotes type 2). From the blocks $5\mu m$ sections were cut and stained using the monoclonal antibody KG9 and lightly counterstained with haematoxylin. All images were acquired with 256 grey-levels using a $\times 10$ magnification factor on a $736 \times 574$ (pixel) frame (see Fig. 12). For each of the vCJD and sporadic CJD cases in the study cohort, 21 features (GTSDM = 9; GLRLM = 7; Fourier = 4; Fractal = 1) were calculated on eight neuropathologically significant regions of interest. Statistical analysis was performed on each feature using the Kruskal-Wallis test. This is a non-parametric test which makes no assumption about the distribution of the data (e.g. normality) and is used to compare three or more independent groups of sampled data. In this work the results were assessed at the 0.05 significance level. In addition, a Mann-Whitney test was used to assess the pair-wise discrimination between groups of sampled data. The hypothesis for the test was that the samples, or feature values, were significantly different between the groups being considered (Nailon et al., 2000).

The Kruskal-Wallis test showed that 18 of the 21 features were able to significantly differentiate between vCJD and sporadic CJD type 1 and 2 at the 0.05 significance level. The Mann-Whitney test, also at the 0.05 significance level, identified that 14 of the 21 features were able to significantly discriminate between the patterns of prion protein deposition found in vCJD and sporadic CJD type 1. The Mann-Whitney test also identified that 14 of the 21 features could significantly discriminate between vCJD and sporadic CJD type 2. It is interesting to note that the combination of GLRLM features found to be significant was different in the assessment of vCJD with sporadic CJD type 1 than vCJD with sporadic CJD type 2. This implies that different combinations of features may be required for different applications. The Mann-Whitney pair-wise significance test between sporadic CJD type 1 and type 2 found no features with significant discriminatory power. The results obtained in the study are summarised in Table 1.

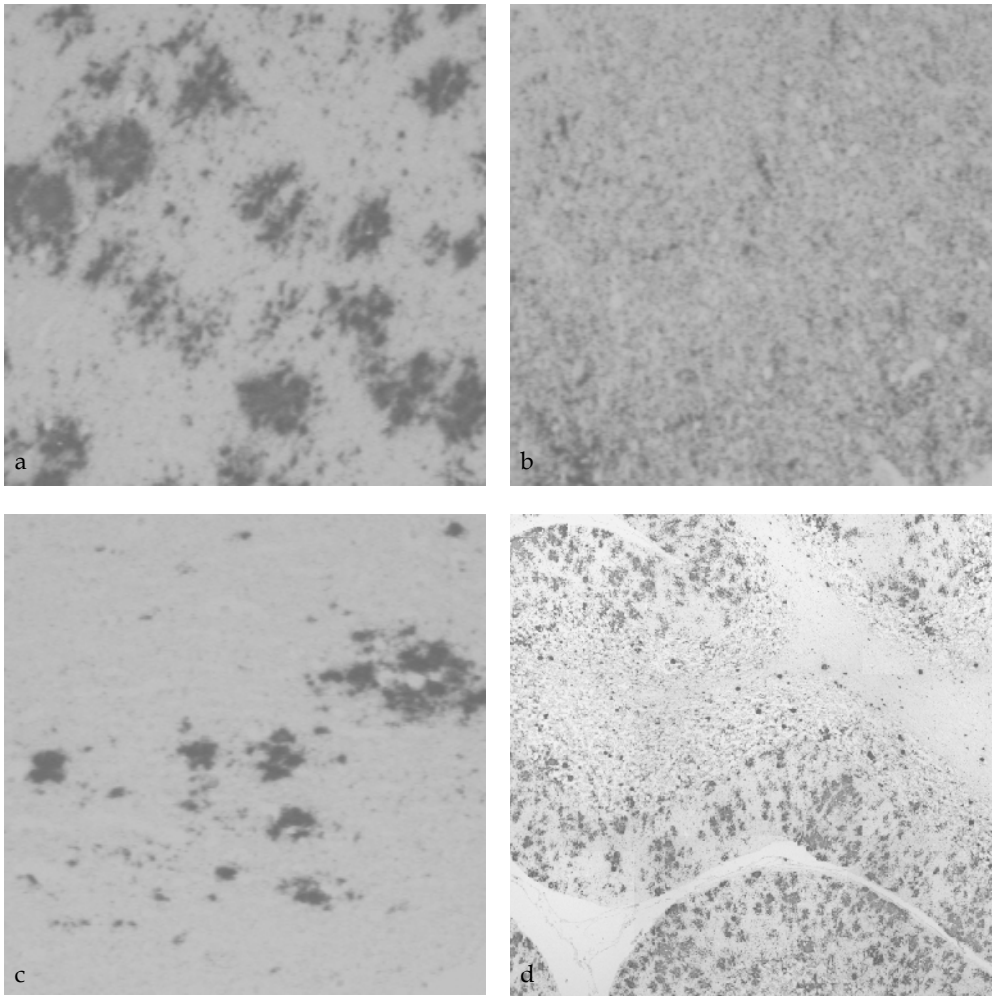


Fig. 12. Microscopic images showing the distribution of prion protein in the molecular layer of the cerebellum of cases of vCJD (a), sporadic CJD type 1 (b) and sporadic CJD type 2 (c). Figure d shows the distribution of prion protein in a larger region formed from nine overlapping microscopic images.

| Feature | Method | Kruskall-Wallis | | Mann-Whitney vCJD/spor CJD t1 | | Mann-Whitney vCJD/spor CJD t2 | | Mann-Whitney spor CJD t1/ spor CJD t2 | |
|---|---|---|---|---|---|---|---|---|---|
| | | Value | Power | Value | Power | Value | Power | Value | Power |
| $f_1$ | GTSDM | 0.052 | - | 0.556 | - | 0.071 | - | 0.057 | - |
| $f_2$ | GTSDM | 0.005 | + | 0.111 | - | 0.036 | + | 0.057 | - |
| $f_3$ | GTSDM | 0.004 | + | 0.016 | + | 0.036 | + | 1.000 | - |
| $f_4$ | GTSDM | 0.050 | + | 0.111 | - | 0.143 | - | 0.114 | - |
| $f_5$ | GTSDM | 0.000 | + | 0.016 | + | 0.036 | + | 0.057 | - |
| $f_6$ | GTSDM | 0.004 | + | 0.016 | + | 0.036 | + | 0.857 | - |
| $f_7$ | GTSDM | 0.002 | + | 0.016 | + | 0.036 | + | 0.400 | - |
| $f_8$ | GTSDM | 0.007 | + | 0.016 | + | 0.571 | - | 0.571 | - |
| $f_9$ | GTSDM | 0.061 | - | 0.016 | + | 0.786 | - | 0.400 | - |
| $f_{10}$ | GLRLM | 0.020 | + | 0.111 | - | 0.143 | - | 0.057 | - |
| $f_{11}$ | GLRLM | 0.065 | - | 0.111 | - | 0.250 | - | 0.114 | - |
| $f_{12}$ | GLRLM | 0.000 | + | 0.016 | + | 0.036 | + | 0.057 | - |
| $f_{13}$ | GLRLM | 0.050 | + | 0.111 | - | 0.143 | - | 0.114 | - |
| $f_{14}$ | GLRLM | 0.050 | + | 0.111 | - | 0.143 | - | 0.114 | - |
| $f_{15}$ | GLRLM | 0.000 | + | 0.016 | + | 0.036 | + | 0.114 | - |
| $f_{16}$ | GLRLM | 0.001 | + | 0.032 | + | 0.036 | + | 0.057 | - |
| $f_{17}$ | Fourier (Ring 1) | 0.002 | + | 0.016 | + | 0.036 | + | 0.400 | - |
| $f_{18}$ | Fourier (Ring 2) | 0.002 | + | 0.016 | + | 0.036 | + | 0.400 | - |
| $f_{19}$ | Fourier (Ring 3) | 0.002 | + | 0.016 | + | 0.036 | + | 0.400 | - |
| $f_{20}$ | Fourier (Ring 4) | 0.002 | + | 0.016 | + | 0.036 | + | 0.400 | - |
| $f_{21}$ | Fractal | 0.004 | + | 0.016 | + | 0.036 | + | 0.857 | - |

Table 1. Power of the features used to discriminate between: vCJD and sporadic CJD type 1; vCJD and sporadic CJD type 2; sporadic CJD type 1 and sporadic CJD type 2. The exact significance value is a measure of the discriminatory power of each feature. (+ indicates good discriminatory power, - indicates poor discriminatory power).

The choice of ring filters used was based on extensive trials on similar data sets. The radii of the final set of filters chosen is summarised in Table 2. The main objective of this work was to use texture analysis to investigate and study the distribution of prion protein found in vCJD and sporadic CJD. All of the Fourier ring features used showed significant discriminatory power in discriminating between vCJD and sporadic CJD types 1 and 2. However, they were unable to discriminate between sporadic CJD types 1 and 2.

| Filter | Inner Radius | Outer Radius |
|---|---|---|
| 1 | $r_1 = 2$ | $r_2 = 5$ |
| 2 | $r_1 = 2$ | $r_2 = 10$ |
| 3 | $r_1 = 5$ | $r_2 = 10$ |
| 4 | $r_1 = 10$ | $r_2 = 20$ |

Table 2. Inner and outer radii of the ring filters used to discriminate between: vCJD and sporadic CJD type 1; vCJD and sporadic CJD type 2; sporadic CJD type 1 and sporadic CJD type 2.

## 7. Summary

Texture analysis methods are useful for discriminating and studying both distinct and subtle textures in multi-modality medical images. Practical implementation requires careful consideration of the power of the individual features to discriminate between textures. This is essential to reduce the influence that heavily correlated features, and features with little discriminatory power, have on the overall classification. Statistical texture analysis techniques are constantly being refined by researchers and the range of applications is increasing. Fractal approaches, which offer the convenience of characterising a textured region by a single measure, appear more application-specific than statistical approaches and require more research. Algorithmic advances have been made on the use of full 3D texture analysis approaches and the publications in this area demonstrate that this is a promising area of research. This is particularly important given that biomedical image data with near isotropic resolution is becoming more common in clinical environments. However, it has been shown that there is minimal loss of discriminatory power when 2D techniques are applied in the coronal and sagittal planes.

## 8. Acknowledgements

The support of Dr. A.T. Redpath, Dr. D.B. McLaren and Professor S. McLaughlin is gratefully acknowledged for helpful discussion and preparation of the results presented in Case Study 1. I am also grateful to Professor J.W. Ironside and Dawn Everington for their assistance in obtaining the results presented in Case Study 2. The support of the laboratory staff at the National CJD Surveillance Unit, UK is acknowledged for preparation of the tissue samples used in Case Study 2. The support of the staff in the NHS Department of Oncology Physics and the School of Engineering at the University of Edinburgh is gratefully acknowledged. The James Clerk Maxwell Foundation is gratefully acknowledged for the provision of financial assistance to continue this work.

## 9. References


Bastian, F.O. (1991). Creutzfeldt-Jakob disease and other transmissible human spongiform encephalopathies. St Louis: Mosby Year Book.

Bajscy, R. (1973). Computer description of textured surfaces, *Proceedings of the Joint Conference on Artificial Intelligence*, August, pp. 572-579.

Brodatz, P. (1966). *Textures: a photographic album for artists and designers.* Dover Publications, ISBN 0-486-40699-7, New York.

Bruce, V.; Georgeson, M. & Green, P. (2003). *Visual Perception: Psychology and Ecology*. Psychology Press Publications, ISBN 1841692387, UK.

Conners, R. & Harlow, C. (1980). Theoretical comparison of texture algorithms. *IEEE Transactions on Pattern Analysis and Machine Intelligence*, Vol. 2, No. 3, pp. 204-222.

Devijver, P.A. & Kittler, J. (1982). *Pattern recognition: a statistical approach*. Prentice Hall, 0-13-654236-0, London.

Distani, R.; Nappi, M. & Riccio, D. (2006). A range/domain approximation error-based approach for fractal image compression. *IEEE Transactions on Image Processing*, Vol. 15, No. 1, pp. 89-97.

Duda, R.; Hart, P. & Stork, D. (2001). Pattern Classification, John Wiley & Sons, ISBN 0-471-05669-3.

Esgiar, A.; Naguib, R.; Sharif, B.; Bennet, M. & Murray, A. (2002). Fractal analysis in the detection of colonic cancer images. *IEEE Transactions on Information Technology in Biomedicine*, Vol. 6, No. 1, pp 54-58.

Feder, J. (1988). *Fractals*. Plenum Press, ISBN 0-306-42851-2, New York.

Galloway, M.M. (1975). Texture analysis using grey-level run lengths. *Computer Graphics and Image Processing*, Vol. 4, pp. 172-179.

Gonzalez, R.C. & Woods, R.E. (2001). *Digital Image Processing*, Prentice Hall, ISBN 0-201-18075-8.

Haralick, R.M.; Shanmugam K. & Dinstein, I. Texture features for image classification. *IEEE Transactions on Pattern Analysis and Machine Intelligence*, Vol. SMC-3, No. 6, Nov 1973, 610-621.

Hartigan, J. (1975). *Clustering Algorithms*. John Wiley & Sons, ISBN 0-471-35645-X.

ICRU, (1999). International Commission on Radiation Units and Measurements. ICRU Report 62: Prescribing, Recording and Reporting Photon Beam Therapy (Supplement to ICRU 50), Oxford University Press.

Ironside, J.W. (1998). Neuropathological findings in new variant Creutzfeldt-Jakob disease and experimental transmission of BSE. *FEMS Immunology & Medical Microbiology*, Vol. 21, No. 2, pp. 91-95.

Ironside, J.W.; Head, M.W.; Bell, J.E.; McCardle, L. & Will, R.G. (2000). Laboratory diagnosis of variant Creutzfeldt-Jakob disease, *Histopathology*, Vol. 37, No. 1, pp. 1-9.

Jain, A.K. & Chandrasekaran. (1982). Dimensionality and sample size considerations. In: *Pattern Recognition in Practice*, Krishnaiah, P.R. & Kanal, L.N., Vol. 2, pp. 835-888. North Holland.

Jain, A.K. & Zongker, D. (1997). Feature selection: evaluation, application and small sample performance. *IEEE Transactions on Pattern Analysis and Machine Intelligence*, Vol. 2, No. 19, pp. 153-158.

Julesz, B. (1975). Experiments in the visual perception of texture. *Scientific American*, Vol. 232, pp 34-43.

Kachouie, N. & Fieguth, P. (2007). A medical texture local binary pattern for TRUS prostate segmentation, *Proceedings of the 29th International Conference of the IEEE Engineering and Biology Society*, Lyon, France, August 23rd – 26th.

Karahaliou, A.; Boniatis, I; Skiadopoulos, S. & Sakellaropoulos, F. (2008). Breast cancer diagnosis: analyzing texture of tissue surrounding microcalcifications. *IEEE Transactions on Information Technology in Biomedicine*, Vol. 12, No. 6, pp. 731-738.

Kovalev, V.; Kruggel, F.; Gertz, H. & von Cramon D. (2001). Three-dimensional texture analysis of MRI brain datasets. *IEEE Transactions on Medical Imaging*, Vol. 20, No. 5, pp. 424-433.

Kurani, A.; Xu, D.; Furst, J. & Raicu, D. (2004). Co-occurrence matrices for volumetric data, *Proceedings of 7th IASTED International Conference on Computer Graphics and Imaging*, Kauai, Hawaii, USA, August 17th – 19th.

Li, L. & Qi, D. (2007) Detection of cracks in computer tomography images of logs based on fractal dimension, *Proceedings of the IEEE International Conference on Automation and Logistics*, pp. 2259-2264, Jinan China, August 18th - 21st .

Mandelbrot, B.B. (1977). *Fractals: form, chance and dimension*. W.H. Freeman and Co., ISBN 0-716-70473-0, New York.

Mirmehdi, M.; Xie, X. & Suri, J. (eds) (2008). *Handbook of texture analysis,* Imperial College Press, 1-84816-115-8, UK.

Meyer, J.L. (ed) (2007). *Frontiers of radiation therapy and oncology (vol 40): IMRT, IGRT, SBRT, advances in the treatment planning and delivery of radiotherapy*, Karger, 978-3-8055-9188-9, Switzerland.

Nailon, W.H. (1997). *Tissue characterisation of intravascular ultrasound using texture analysis*. Ph.D. dissertation, The University of Edinburgh, School of Engineering.

Nailon, W.H.; Everington, D. & Ironside, J.W. (2000). *Prion protein characterisation by image analysis*. Internal communication, National CJD Surveillance Unit, Edinburgh, UK.

Nailon, W.H. & Ironside, J.W. (2000) Variant Creutzfeldt-Jakob disease: immunocytochemical studies and image analysis. *Microscopy Research & Technique*, Vol. 50, No. 1, pp. 2-9.

Nailon, W.H.; Redpath, A.T. & McLaren, D.B. (2008). Characterisation of radiotherapy planning volumes using textural analysis. *Acta Oncologica*, Vol. 47, pp. 1303-1308.

Nouza, J. (1995). On the speech feature selection problem: are dynamic features more important than static ones? *Proceedings of the European Conference on Speech Communication and Technology*, pp 917-921, Madrid, Spain, September.

Peitgen, H. & Saupe, D. (1988). *The science of fractal images.* Springer-Verlag, ISBN 0-387-96608-0, New York.

Peitgen, H.; Jurgen, H. & Saupe, D. (1992). *Chaos and fractals: new frontiers of science*. Springer-Verlag, ISBN 0-387-97903-4, New York.

Pietikainen, M.K. (ed) (2000). *Texture analysis in machine vision*, World Scientific Publishing, 981-02-4373-1, Singapore.

Pentland, P. (1984). Fractal-based description of natural scenes. *IEEE Transactions on Pattern Analysis and Machine Intelligence*, Vol. PAMI-6, No. 6, Nov, pp. 661-674.

Podda, B.; Zanetti, G. & Giachetti, A. (2005). Texture analysis for vascular segmentation from CT images, *Proceedings of Computer Assisted Radiology and Surgery (CARS)*, pp. 206-211, Berlin, Germany, 22nd-25th June, 2005.

Pratt, W.K. (1978). *Digital Image Processing*, John Wiley & Sons, 0-471-01888-0, New York.

Press, W.; Flannery, B.; Teulkolsky, S. & Vetterling, W. *Numerical recipes in C: the art of scientific computing*. Cambridge University Press, ISBN 0-521-35465-X, UK.

Russ, J.C. (1994). *Fractal surfaces*. Plenum Press, ISBN 0-306-44702-9, New York.

Sammon, J. (1969). A nonlinear mapping for data structure analysis. *IEEE Transactions on Computing*, Vol, C-18, pp. 401-409.

Steenbakkers, R.J.H.M.; Duppen, J.C.; Fitton, I.; Deurloo, K.E.I.; Zijp, L.; Uitterhoeve A.L.J.; Rodrigus P.T.R.; Kramer, G.W.P.; Bussink, J.; De Jaeger, K.; Belderbos, J.S.A.; Hart, A.A.M.; Nowak, P.J.C.M.; van Herk, M. & Rasch, C.R.N. (2005). Observer variation in target volume delineation of lung cancer related to radiation oncologist-computer interaction: a 'big-brother' evaluation. *Radiotherapy & Oncology,* Vol. 77, pp. 182-190.

Stearns, S.D. (1976). On selecting features for pattern classifiers. *In Proceedings of the 3rd International Conference on Pattern Recognition*, pp. 71-75, Colorado, USA.

Stoyan, D. & Stoyan, H. (1994). *Fractals, random shapes and point fields: methods of geometrical statistics*. John Wiley & Sons, ISBN 0-471-93757-6, New York.

Therrien, C.W. (1989). *Decision estimation and classification: an introduction to statistical pattern recognition and related topics*, John Wiley & Sons, 0-471-83102-6, New York.

Tuceryan, M. & Jain, A.K. (1998). Texture analysis. In: Chen, C.H; Pau, L.F. & Wang, P.S.P., (eds). *The handbook of pattern recognition and computer vision*. 2nd ed. World Scientific Publishing Co., ISBN 9-810-23071-0, Singapore.

Turcotte, D.L. (1992). *Fractals and Chaos in Geology and Geophysics*, Cambridge University Press, ISBN 0-521-56164-7, Cambridge, UK.

Uppaluri, R.; Mitsa, T.; Sonka, M.; Hoffman, E. & McLennan G. (1997). Quantification of pulmonary emphysema from lung computed tomography images. *American Journal of Respiratory Care in Medicine*, Vol. 156, No. 1, pp. 248-254.

Weber, A.G. (2004). The USC texture mosaics. *University of Southern California Viterbi School of Engineering*, http://sipi.usc.edu/ .

Weltons, C.; Menten, J.; Feron, M.; Bellon, E.; Demaerel, P.; Maes, F.; van den Bogaert, W. & van der Schueren, E. (2001). Interobserver variations in gross tumor volume delineation of brain tumours on CT and impact of MRI. Radiotherapy & Oncology, Vol. 60, No. 1, pp. 49-59.

Winzenrieth, R. & Claude, I. (2006). Is there functional vascular information in anatomical MR sequences? A preliminary in vivo study. *IEEE Transactions on Biomedical Engineering*, Vol. 53, No. 6, June 2006, pp.1190-1194.

Xu, D.; Kurani, A. & Raicu, D. (2004). Run-length encoding for volumetric texture, *Proceedings of 4th IASTED International Conference on Visualization, Imaging and Image Processing – VIIP,* Marbella, Spain, September 6th – 8th.

Xu, Y.; Sonka, G.; McLennan, G.; Junfeng, G. & Hoffman, E. (2006). MDCT-based 3D texture classification of emphysema and early smoking related pathologies. *IEEE Transactions on Medical Imaging*, Vol. 25, No. 4, pp. 464-475.

Yu, H.; Caldwell, C.; Mah, K. & Mozeg D. (2009). Co-registered FDG PET/CT based textural characterization of head and neck cancer in radiation treatment planning. *IEEE Transactions on Medical Imaging*, Vol. 28, No. 3, pp. 374-383.

Yu, Z.; Jixian, Z. & Haitao, L. (2007). Fractal characteristics of very high resolution satellite imagery, *Proceedings of Geoscience and Remote Sensing Symposium*, pp. 389-92, Barcelona, Spain, July 23rd-27th.

Zhou, B.; Xuan, J.; Zhao, H.; Chepko, M.; Freedman, M. & Yingyin, K. (2007). Polarization imaging for breast cancer diagnosis using texture analysis and svm, Proceedings of Life Sciences Systems and Applications Workshop, pp. 217-220, Bethesda, Maryland, USA.

Zonger, D. & Jain, A. (1996). Algorithms for feature selection: an evaluation. *Proceedings of the 13th International Conference on Pattern Recognition (ICPR'96)*, Vol. B, pp. 18-22, Vienna, Austria, August.

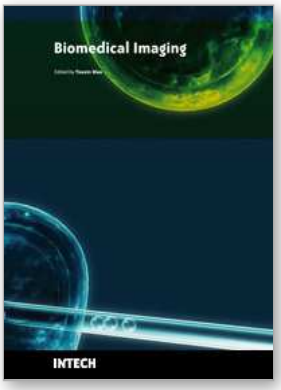


**Biomedical Imaging**

Edited by Youxin Mao

ISBN 978-953-307-071-1
Hard cover, 100 pages
**Publisher** InTech
**Published online** 01, March, 2010
**Published in print edition** March, 2010

Biomedical imaging is becoming an indispensable branch within bioengineering. This research field has recently expanded due to the requirement of high-level medical diagnostics and rapid development of interdisciplinary modern technologies. This book is designed to present the most recent advances in instrumentation, methods, and image processing as well as clinical applications in important areas of biomedical imaging. It provides broad coverage of the field of biomedical imaging, with particular attention to an engineering viewpoint. The goal of the book is to provide a wide-ranging forum in the biomedical imaging field that integrates interdisciplinary research and development of interest to scientists, engineers, teachers, students, and clinical providers.



**InTech Europe**
University Campus STeP Ri
Slavka Krautzeka 83/A
51000 Rijeka, Croatia
Phone: +385 (51) 770 447
Fax: +385 (51) 686 166
www.intechopen.com

**InTech China**
Unit 405, Office Block, Hotel Equatorial Shanghai
No.65, Yan An Road (West), Shanghai, 200040, China
中国上海市延安西路65号上海国际贵都大饭店办公楼405单元
Phone: +86-21-62489820
Fax: +86-21-62489821